Contributed Paper

Electron Pressure Profiles in High-Density Neutral Beam Heated Plasmas in the Large Helical Device

MIYAZAWA Junichi[i], YAMADA Hiroshi[i], PETERSON Byron J.[i], MURAKAMI Sadayoshi[ii],
FUNABA Hisamichi[i], OSAKABE Masaki[i], TANAKA Kenji[i],
SAKAKIBARA Satoru[i] and LHD Experimental Group

[i] *National Institute for Fusion Science, 322-6 Oroshi-cho, Toki, 509-5292, Japan*
[ii] *Department of Nuclear Engineering, Kyoto University, Kyoto, 606-8501, Japan*

(Received 2 September 2004 / Accepted 11 March 2005)

In the Large Helical Device (LHD), electron pressure profiles in gas-fueled high-density discharges tend to have a similar shape, as if these were frozen. This frozen profile is insensitive to variations in the magnetic field strength and moderate changes in the neutral beam heat deposition profile. At the same time, however, the absolute value of the electron pressure itself increases with the heating power, the electron density, and the magnetic field strength. In this study, a reference model for the electron pressure is proposed which consists of the frozen profile and parametric dependences derived from experimental observations. It is possible to define an operational regime where this typical profile appears by comparing the electron pressure profiles with this model. In the standard configuration, at which the maximum plasma stored energy in LHD has been obtained, the frozen profile appears in the plateau to the Pfirsch-Schlüter regimes. As the collisionality decreases to the collisionless regime, the electron pressure becomes smaller than the prediction of the model and the deterioration is significant in the plasma core region. This tendency is enhanced in the configuration with the outward-shifted magnetic axis. The global energy confinement time, τ_E, in the high-collisionality regime has a weaker density dependence together with the mitigated power degradation, scaling as $\tau_E \propto \bar{n}_e^{0.28} P^{-0.43}$ ($\bar{n}_e$ and P are the line-averaged density and the heating power, respectively), compared with the International Stellarator Scaling 95, where $\tau_E \propto \bar{n}_e^{0.51} P^{-0.59}$.

Keywords:
LHD, high-density, plateau regime, frozen profile, stiffness, energy confinement

1. Introduction

The confinement property of high-temperature plasmas in the high-density region is one of the important physics subjects in fusion reactor oriented studies, since high-density operation is favorable for achieving a higher fusion triple product. On the other hand, many examples of confinement degradation in the high-density region have been reported from both of tokamak and helical plasma experiments [1-4]. Use of empirical scaling laws for the energy confinement time, τ_E, is effective to identify the data deviating from the typical expectation, possibly due to a degradation or improvement of confinement. For example, the international stellarator scaling 95 (ISS95) [5] has been widely used to discuss the energy confinement of stellarators including the Large Helical Device (LHD) [6-9]. The energy confinement time predicted by the ISS95 scaling, τ_E^{ISS95}, has a favorable positive density dependence,

$$\tau_E^{\mathrm{ISS95}} = 0.079\, a^{2.21} R^{0.65} P_{\mathrm{tot}}^{-0.59} \bar{n}_e^{0.51} B_t^{0.83} \bar{\iota}_{2/3}^{0.4}\,, \quad (1)$$

where a, R, P_{tot}, $\bar{n}_e$, B_t, and $\bar{\iota}_{2/3}$ denote the minor radius (m), major radius (m), total heating power (MW), line-averaged electron density (10^{19} m^{-3}), magnetic field strength (T), and rotational transform at $\rho = r/a = 2/3$, respectively [5]. At a fixed heating power, therefore, the plasma-stored energy is expected to increase with the density. Indeed, this tendency is recognized in gas-fueled LHD plasmas in the moderate density region [10]. It is also observed, however, that the strong positive density dependence is lost in the high-density region during the density ramp-up by gas puffing. The energy confinement time in such a case is lower than the prediction of scalings with significant density dependence [3,4].

In this study, confinement properties of gas-fueled neutral beam (NB) heated LHD plasmas in the high-density region are investigated. It will be shown that the significant positive density dependence as given by ISS95 declines in the high-density region and that electron pressure profiles tend to have a similar shape. The typical profile, which is insensitive to variations in the experimental conditions, will be called a “frozen profile”. In such a case, the profile of the scale length of the electron pressure gradient converges to a

---

author’s e-mail: miyazawa@lhd.nifs.ac.jp typical curve. This is analogous to the stiffness observed in tokamaks, where the temperature gradient scale length is robust to the change in the heating deposition profile. This inevitably occurs if the thermal diffusivity, χ, has a nonlinear positive dependence on the temperature, T, as $\chi \propto T^{\alpha}$ ($\alpha > 0$), for example, since the electron temperature scarcely increases with the heating power due to the simultaneous increase in the thermal diffusivity. In other words, profile stiffness implies the non-linear dependence(s) of the thermal diffusivity. Studies of profile stiffness have been intensively pursued in tokamaks [1,2,11-16]. In these studies, stiffness in the temperature profile has been mainly discussed in relation to the ion temperature gradient mode [11-13] or the electron temperature gradient mode [14-16]. So-called transient transport analysis enables one to identify the nonlinear temperature gradient dependence of χ [17]. Comparison of the heat pulse diffusivity, χ^{HP}, with that from power balance analysis, χ^{PB}, indicates that a strong temperature gradient dependence appears ($\chi^{\mathrm{HP}} \gg \chi^{\mathrm{PB}}$) when the temperature gradient exceeds a critical value [16]. The ratio $\chi^{\mathrm{HP}}/\chi^{\mathrm{PB}}$ is called the “stiffness parameter”, since such a nonlinear dependence of χ can cause the stiffness. As for the stellarators, on the other hand, studies in Wendelstein 7-AS [18-21] have shown that no systematic discrepancy between χ^{HP} and χ^{PB} is found [19,21] and therefore strong temperature gradient dependence can be ruled out. The transient transport analysis has been also applied to LHD plasmas with an electron internal transport barrier (e-ITB) [22-24]. It has been shown that the electron thermal diffusivity increases with $T_{\mathrm{e}}^{1.6}$ outside of the e-ITB [23], which is similar to the gyro-Bohm model, while the dependence on the temperature gradient seems negligibly small [24]. Note that the experimental regime is limited to low-density in these studies, since low collisionality is required to achieve the e-ITB [22]. In the present study, the electron pressure profile is highlighted to investigate the global energy confinement property in NB heated plasmas in LHD. The energy confinement time is readily obtained from the electron pressure profile, while the temperature profile alone is not enough to discuss the global energy confinement. However, the pressure gradient is mainly determined by the temperature gradient in our case, since our database is extracted from gas puff experiments where the density gradient is small except in the plasma edge region. It also should be noted that electron heating is dominant in LHD, where high-energy neutral beam injection is adopted.

2. Apparatus

LHD is the largest super-conducting helical device in the world [6-9]. The major radius of the toroidal vacuum vessel is 3.9 m, and the maximum magnetic field strength at the plasma center is ~ 3 T. This study deals with gas-fueled hydrogen plasmas in a standard configuration of $R_{\mathrm{ax}} = 3.6$ m, or an outward-shifted configuration of $R_{\mathrm{ax}} = 3.75$ m, where R_{ax} denotes the major radius of magnetic axis in the vacuum configuration. Each of the magnetic configurations has unique properties, *e.g.* neo-classical transport is reduced in $R_{\mathrm{ax}} = 3.6$ m compared with the outward-shifted configurations [25] and especially the trajectories of the high-energy trapped particles are well aligned with the magnetic surfaces [26], while better MHD stability is expected in the outward-shifted configurations that have a magnetic well [27]. Furthermore, the largest confinement volume of ~ 30 m^3 is obtained in $R_{\mathrm{ax}} = 3.6$ m and the maximum plasma stored energy of 1.3 MJ has been achieved in this configuration [28].

The main heating system in LHD is negative-ion based neutral beam (NB) injection, which consists of three beam lines. The beam energy ranges from 140 to 180 keV, which is much higher than the typical electron temperature of a few keV in NB heated plasmas. Therefore, electron heating is dominant (typically, 80–90 % of total heating power is deposited to electrons). Although the heating power of each beam line is fixed, combinations of the three beam lines enable a power scan experiment, where the total port-through power of NB, $P_{\mathrm{NB}}^{\mathrm{PT}}$, is varied. The NB heating power, P_{NB}, is estimated from $P_{\mathrm{NB}}^{\mathrm{PT}}$ and direct heat load measurements of NB shine-through power on the armor plates [29]. Note that P_{NB} is smaller than $P_{\mathrm{NB}}^{\mathrm{PT}}$ especially in the low-density region where the fraction of NB shine-through is large. Furthermore, due to the deviation of the high-energy beam trajectory from the magnetic surfaces, prompt loss of beam ions is expected other than the beam shine-through, which is not included in P_{NB}. This prompt loss is calculated by the FIT code [30] to give an NB heat deposition profile, $P_{\mathrm{dep}}(\rho)$, where $\rho = r/a$ is the normalized radius and a is the averaged minor radius of the last closed flux surface.

In this study, the confinement property of NB heated LHD plasmas is discussed based on the analysis of electron pressure profiles, $p_{\mathrm{e}}(\rho)$. The $p_{\mathrm{e}}(\rho)$ is given as a product of the electron temperature, $T_{\mathrm{e}}(\rho)$, and the electron density, $n_{\mathrm{e}}(\rho)$, where $T_{\mathrm{e}}(\rho)$ is measured by Thomson scattering [31] and $n_{\mathrm{e}}(\rho)$ is estimated from Abel inversion of multi-chord far-infra-red interferometer signals [32]. Here the projection to ρ has been performed using equilibria calculated by the VMEC code [33].

3. Frozen Profile

To study the parameter dependence of the energy confinement in the high density region, NB power scan experiments have been performed, where $P_{\mathrm{NB}}^{\mathrm{PT}}$ is scanned from 3 to 10 MW while the magnetic configuration is fixed to R_{ax} / B_0 = 3.6 m / 1.5 T (Fig. 1). At each $P_{\mathrm{NB}}^{\mathrm{PT}}$, $\overline{n}_{\mathrm{e}}$ is scanned by gas puffing. The electron stored energy, $W_{\mathrm{e}}^{\mathrm{exp}}$, increases with $\overline{n}_{\mathrm{e}}$(Fig. 1(b)) in the low-density region of $\overline{n}_{\mathrm{e}} < 3 \times 10^{19}$ m^{-3}. In this region, $W_{\mathrm{e}}^{\mathrm{exp}}$ agrees well with the trend of ISS95. In the high-density region, however, $W_{\mathrm{e}}^{\mathrm{exp}}$ stops increasing (see hatched density region in Fig. 1) and even decreases at higher density near the operational density limit (beyond the hatched density region) [34,35]. The hatched density region of $3.5 < \overline{n}_{\mathrm{e}}(10^{19}$ m$^{-3}) < 5.5$ in Fig. 1 is arbitrarily determined since the threshold density, where the strong positive density dependence of $W_{\mathrm{e}}^{\mathrm{exp}}$ at a fixed heating power is lost, is ambiguous and the operational density limit varies with the heating power. Although the strong positive density dependence is lost in this region, W_e^{exp} and the local electron pressure (Figs. 1(b) and 1(c)) still increase with the heating power. One might notice that W_e^{exp} plotted by the squares and the diamonds, which correspond to P_{NB}^{PT} = 7 and 6 MW, respectively, are similar at $\overline{n}_e \sim 5 \times 10^{19}$ m^{-3}, in spite of the different heating power. This will be discussed later in section 4.1. To discuss the change in confinement property, it is important to know the electron pressure gradient, $dp_e/d\rho$, and its scale length, $L_p = (-d(\ln p_e)/d\rho)^{-1}$. In Fig. 1(d), shown are the density dependence of L_p^{-1} at ρ = 0.6 and 0.8. An important characteristic emerges from this figure, *i.e.* L_p is constant within ±10 % in the hatched density region, in spite of 4 times difference in P_{NB} (2.5 – 10 MW) and, correspondingly, 2 times difference in local p_e. In the low-density region, L_p is not constant.

Radial profiles of L_p^{-1} in the high-density region, where the strong positive density dependence of τ_E is lost, are shown in Fig. 2(a). The magnetic configuration is fixed to R_{ax} = 3.6 m, while B_0 is varied from 0.65 T to 2.75 T. Although each of these time slices has a different density (2 – 10 × 10^{19} m^{-3}), NB heating power (2 – 12 MW), and NB deposition profiles as summarized in Table 1 and Fig. 2(b), the L_p profile scarcely changes (Fig. 2(a)). The collisionalities, ν_p^*, in these time slices are high (0.17 ~ 1.07 at ρ = 0.9, see Table 1) and in the plateau or the Pfirsh-Schlüter (P-S) regimes, where $\nu_p^* = \nu_{ei}R_{ax}/(v_T^e(\iota/2\pi))$ (ν_{ei}, v_T^e, and ι denote electron-ion collision frequency, electron thermal speed, and rotational transform,

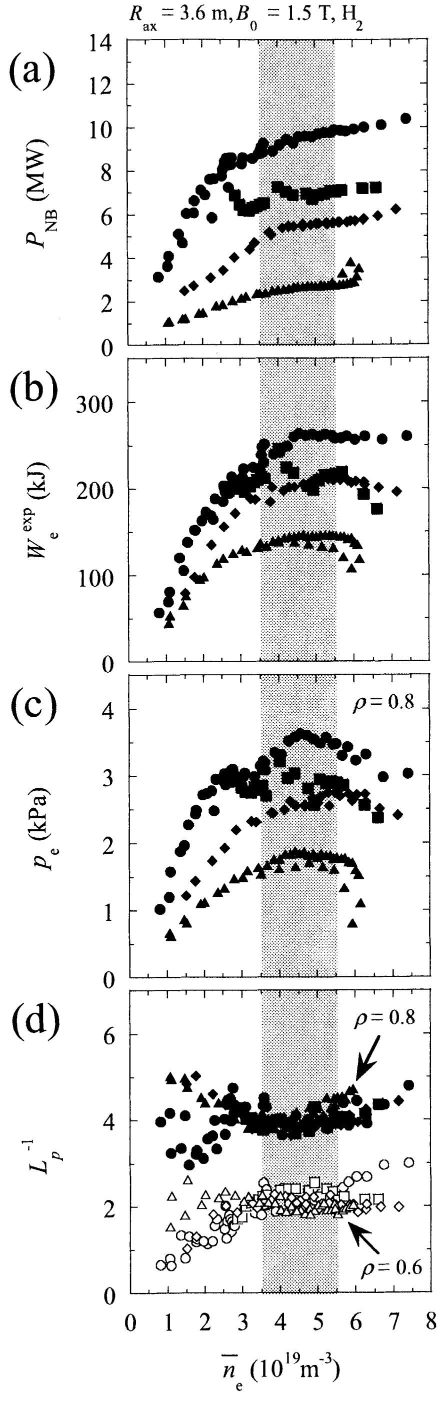

Fig. 1 Summary of the NB heating power scan experiment consisting of data from seven discharges, where (a) the NB heating power, P_{NB}, (b) the electron stored energy, W_e^{exp}, (c) the electron pressure, p_e, at ρ = 0.8, and (d) the characteristic length of the electron pressure gradient, L_p^{-1}, at ρ = 0.6 (open symbols) and ρ = 0.8 (closed symbols), are shown from top to bottom. Circles, squares, diamonds, and triangles denote P_{NB}^{PT} ~ 10, 7, 6, and 3 MW, respectively. Note that P_{NB} in (a) is smaller than the corresponding P_{NB}^{PT} especially in the low-density region due the large fraction of the beam shine-through power. The frozen profile appears in the hatched density region.

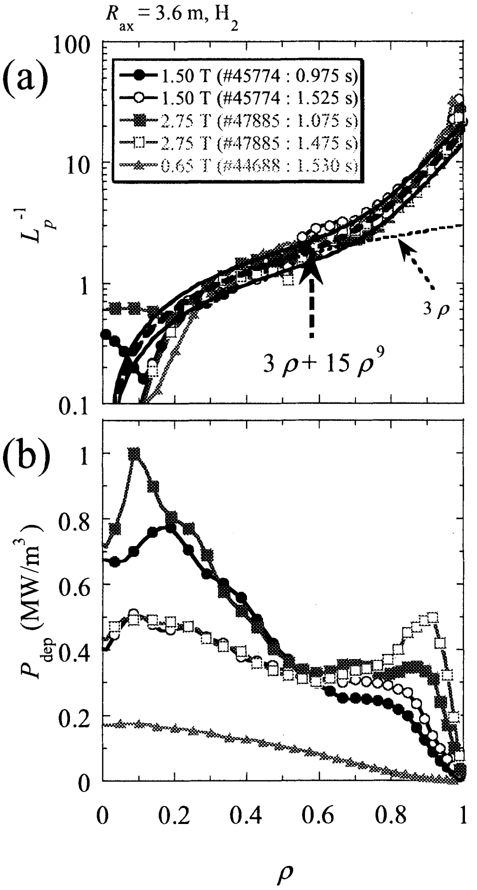

Fig. 2 Radial profiles of (a) the characteristic length of the electron pressure gradient at various magnetic field strengths, and (b) the NB heat deposition.

Table. 1 Typical plasma parameters in the time slices shown in Fig. 2.

Shot number	Time (s)	B_0 (T)	$\bar{n}_e(10^{19}\ \mathrm{m}^{-3})$	P_{NB} (MW)	ν_p^* ($\rho = 0.9$)
#45774	0.975	1.50	4.3	2.6	0.52
#45774	1.525	1.50	5.5	2.8	1.07
#47885	1.075	2.75	7.2	11.1	0.17
#47885	1.475	2.75	10.0	11.9	0.57
#44688	1.530	0.65	2.3	2.1	0.72

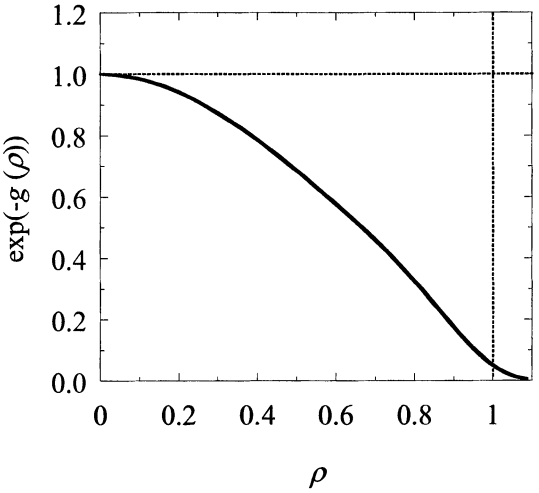

Fig. 3 The base electron pressure profile determined from the frozen L_p profiles shown in Fig. 2(a).

respectively, and $\nu_p^* = 1$ corresponds to the boundary between the plateau and the P-S regimes. In typical cases, ν_p^* in the central region ($\rho < 0.3$) is about one tenth of that at $\rho = 0.9$ and monotonically increases with ρ). The conspicuous character observed in Fig. 1(d) can now be extended in that the L_p in the high-collisionality regime is insensitive to the magnetic field strength and the NB heat deposition profiles. Interestingly, a similar profile has been found in the temperature characteristic length, L_T, in L-mode tokamak plasmas of DIII-D [14] and ASDEX-U [16], although these stiff profiles tend to be flat around $\rho \sim 0.5$ in some cases. Note that, however, the stiffness in tokamaks appears in the high-temperature regime ($T_e > 0.8$ keV) [16].

The L_p profile in the high-collisionality regime can be fitted by a function of ρ, $g'(\rho) = 3\rho + 15\rho^9$, as shown in Fig. 2(a). Typically, L_p^{-1} at $0.3 < \rho < 0.9$ is reproduced by $g'(\rho)$ within 20 % as is shown by the solid lines in the figure. It is possible to reproduce the electron pressure profiles in the high-collisionality regime using the following equations;

$$p_e(\rho) = F \exp(-g(\rho)) , \tag{2}$$

$$g(\rho) = 1.5\rho^2 + 1.5\rho^{10} . \tag{3}$$

The factor F is primarily a function of the heating power, which will be determined in the next section. Here we call $\exp(-g(\rho))$ a frozen profile, which is depicted in Fig. 3. The volume integral of the frozen profile is defined as the base electron-stored energy, W_e^{base}, i.e.

$$W_e^{\mathrm{base}} = \int_0^1 \exp(-g(\rho)) \cdot V' \mathrm{d}\rho , \tag{4}$$

where $V' = \mathrm{d}V/\mathrm{d}\rho$ is the radial derivative of the specific volume.

4. Parameter Dependences of the Model

4.1 Heating power dependence

Even though the pressure profile is frozen, the electron pressure itself (and $W_e^{\exp}$) increases with the NB heating power (see Fig. 1). A normalized electron stored energy, $W_e^{\exp}/W_e^{\mathrm{base}}$, is fitted by $f_P = 3.3P_{\mathrm{tot}}^{0.55}$, as shown in Fig. 4(a), where P_{tot} (MW) $= P_{\mathrm{NB}} - \mathrm{d}W_p^{\mathrm{dia}}/\mathrm{d}t$ and W_p^{dia} is the plasma stored energy estimated from diamagnetic signals. In our database, $\mathrm{d}W_p^{\mathrm{dia}}/\mathrm{d}t$ is small and less than 10 % of P_{tot} at most. Data extracted from the density region of $3.5 < \bar{n}_e(10^{19}\ \mathrm{m}^{-3}) < 5.5$, which corresponds to the hatched region in Fig. 1, are used to obtain the fitting function. Models of the electron pressure profile and the electron-stored energy (model A) are then given by;

$$\begin{aligned} p_e^{\mathrm{modelA}}(\rho) &= f_P \exp(-g(\rho)) \\ &= 3.3P_{\mathrm{tot}}^{0.55} \exp(-(1.5\rho^2 + 1.5\rho^{10})) , \end{aligned} \tag{5}$$

$$W_e^{\mathrm{modelA}} = f_P\, W_e^{\mathrm{base}} . \tag{6}$$

The NB heating power deposition profile changes with the experimental condition, as was shown in Fig. 2(b). Apparently, a higher p_e profile is achieved in the central heating cases [3], although the profile shape, or the L_p profile, is frozen. Such an example is shown in Fig. 5, where two time slices at different densities are chosen from a discharge. These were also indicated in Fig. 2, as typical examples of the frozen L_p profiles in different experimental conditions. Broken lines show the profiles when the NB heat deposition is centrally peaked, while the gray solid lines show the higher density case where the NB heat deposition profile is flat. Since the heat flux in the core region should be more important than that at $\rho = 1$, we have adopted an averaged NB heat flux, $Q_{\mathrm{NB}}^{\mathrm{avg}}$ (MW/m^2), as an index of the NB heating power instead of P_{tot}, where $Q_{\mathrm{NB}}^{\mathrm{avg}}$ is the line-averaged value of the approximated NB heat flux profile defined as below.

$$Q_{\mathrm{NB}}(\rho) = P_{\mathrm{dep}}^{\mathrm{V}}(\rho)/(4\pi^2\rho\, aR_{\mathrm{ax}}) , \tag{7}$$

$$P_{\mathrm{dep}}^{\mathrm{V}}(\rho) = \int_0^\rho P_{\mathrm{dep}}(\rho) \cdot V' \mathrm{d}\rho . \tag{8}$$

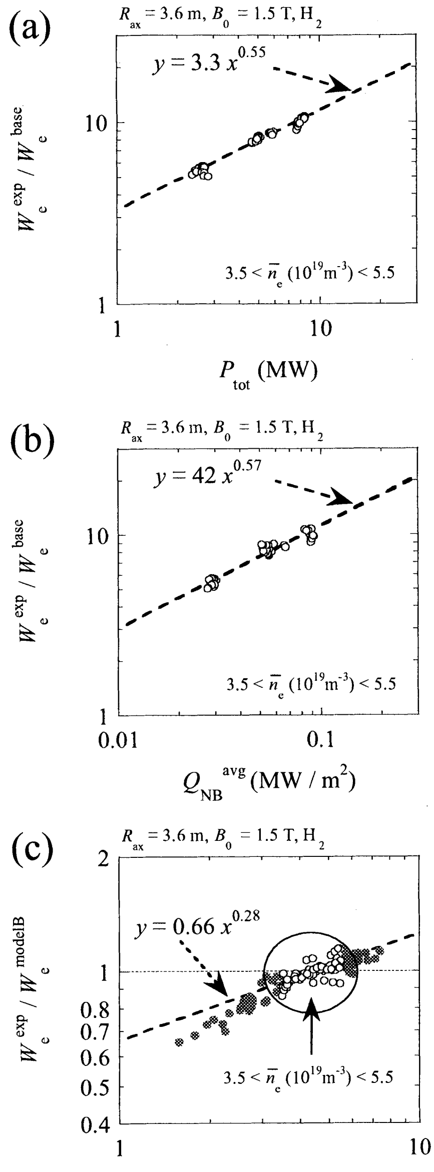

Fig. 4 (a) Heating power dependence of W_e^{exp}, (b) Q_{NB}^{avg} dependence of W_e^{exp}, and (c) density dependence of W_e^{exp}/W_e^{modelB}. Open circles are extracted from the hatched density region in Fig. 1.

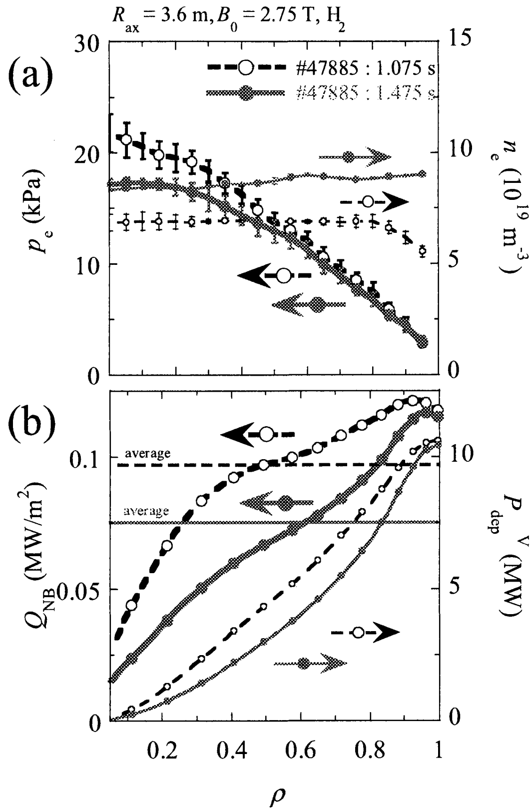

Fig. 5 Radial profiles of (a) electron pressure and electron density, (b) NB heat flux and volume integrated NB heat deposition, at different density. Straight lines in (b) denote the line-averaged NB heat flux. At higher density (gray solid lines), the electron pressure is smaller than that at the lower density (broken lines). Line-averaged NB heat flux is also smaller in the high-density case, although the total deposited power (P_{dep}^V ~ 10 MW at ρ = 1) is similar.

Although the P_{dep}^V at $\rho = 1$, which equals P_{tot} as long as the prompt loss of beam ions and dW_p^{dia}/dt are negligible, is similar for both cases, higher p_e is obtained in the central heating case, where Q_{NB} is 30 % higher at $0.3 < \rho < 0.8$ (the L_p^{-1} profiles in both cases are similar to $g'(\rho)$ within ±10 %). Here we adopt the line-average of Q_{NB} as representative of the heating power for simplicity. It is possible to chose Q_{NB} at a specific ρ, such as ρ ~ 0.6, which corresponds to the centroid of the volume integration of the electron pressure. However, line-average would be better since use of Q_{NB} at a specific ρ underestimates the heating power in the case of off-axis electron cyclotron heating outside of ρ, for example, although such plasmas are not included in this study. As long as the heat deposition profile is smooth as shown in Fig. 5(b), Q_{NB}^{avg} is similar to Q_{NB} at ρ ~ 0.6. As $\bar{n}_e$ increases, the NB heat deposition profile changes from centrally peaked to flat, which can be seen in the $\bar{n}_e$ dependence of $Q_{NB}^{avg}/P_{dep}^V(\rho = 1)$, as shown in Fig. 6.

Returning to Fig. 1 (b), where W_e^{exp} of 200 kJ is obtained within ±10 % at $3.5 < \bar{n}_e(10^{19}\ \mathrm{m}^{-3}) < 5.5$ in spite of 30 % difference in P_{NB} (squares for P_{NB} ~ 7 MW and diamonds for P_{NB} ~ 5.5 MW in the figure), these two have different NB heat deposition profiles but similar Q_{NB}^{avg} (within 5 %). Therefore, use of Q_{NB}^{avg} instead of P_{tot} is effective to reproduce W_e^{exp}. As shown in Fig. 4(b), W_e^{exp}/W_e^{base} can be fitted with $42(Q_{NB}^{avg})^{0.57}$, in the density region of $3.5 < \bar{n}_e(10^{19}\ \mathrm{m}^{-3}) < 5.5$. Then we have model B as

$$p_e^{modelB}(\rho) = f_P^Q \exp(-g)\ , \tag{9}$$

$$W_e^{modelB} = f_P^Q\ W_e^{base}\ , \tag{10}$$

$$f_P^Q = 42(Q_{NB}^{avg})^{0.57}\ . \tag{11}$$

Weak positive density dependence exists in W_e^{exp}/W_e^{modelB}, as depicted in Fig. 4 (c). This density dependence has the form of $f_n = 0.66\ \bar{n}_e^{0.28}$, in the density region of $3.5 < \bar{n}_e(10^{19}\ \mathrm{m}^{-3})$

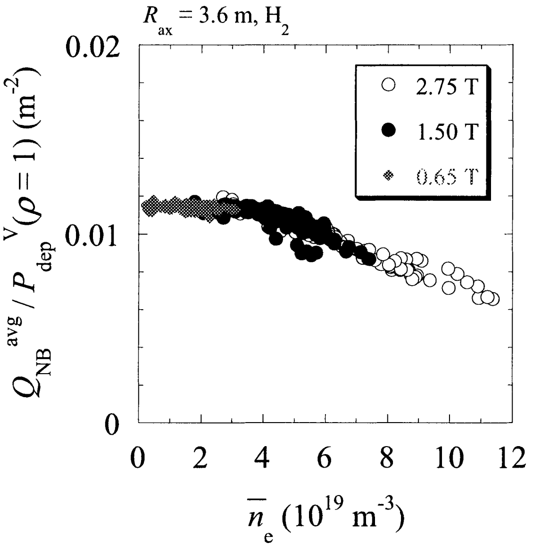

Fig. 6 Line-averaged NB heat flux, Q_{NB}^{avg}, normalized by the total deposited power, $P_{dep}^{V}(\rho = 1)$, with respect to the line-averaged electron density. As the density increases, beam penetration depth becomes shallow and $Q_{NB}^{avg}/P_{dep}^{V}(\rho = 1)$ decreases.

< 5.5. Using this, the third model is derived as

$$p_e^{\mathrm{modelC}}(\rho) = f_n f_P^Q \exp(-g)\,, \tag{12}$$

$$W_e^{\mathrm{modelC}} = f_n f_P^Q W_e^{\mathrm{base}}\,. \tag{13}$$

These three models are composed of the frozen profiles. In other words, it is possible to determine the operational region where the frozen profile appears by comparing the electron pressure profiles with these models.

4.2 Magnetic field dependence

Models A, B, and C are compared with the experimental data of W_e^{exp} in Fig. 7, where datasets taken at B_0 = 1.5 and 2.75 T are shown (R_{ax} is fixed to 3.6 m). The abscissa is given by ν_p* at ρ = 0.9. At B_0 = 1.5 T, all models reproduce W_e^{exp} within ±10% in the high-density and high-collisionality region (hatched in Fig. 7). As the collisionality decreases ($\nu_p*(\rho = 0.9) < 0.1$), W_e^{exp} becomes smaller than the prediction of the models. This corresponds to the low-density region of $\bar{n}_e < 3 \times 10^{19}$ m^{-3} in Fig. 1. Precisely speaking, model C slightly overestimates W_e^{exp} of B_0 = 1.5 T in the P-S regime ($\nu_p* (\rho = 0.9) > 1$). This might be due to the large fraction of the radiation loss, which increases up to ~ 30 % of the total heating power in the same density region until the discharge is terminated by radiative collapse [35].

Qualitatively a similar tendency can also be recognized in the other dataset of B_0 = 2.75 T, although the ratio systematically increases with B_0. This suggests a hidden B_0 dependence in the models. The ratio $W_e^{\mathrm{exp}}/W_e^{\mathrm{modelC}}$ in the high collisionality regime ($\nu_p* (\rho = 0.9) > 0.1$) is plotted against B_0 in Fig. 8. As shown in the figure, $W_e^{\mathrm{exp}}/W_e^{\mathrm{modelC}}$ is fitted by $f_B = 0.76\, B_0^{0.74}$. A corrected version of model C is introduced as,

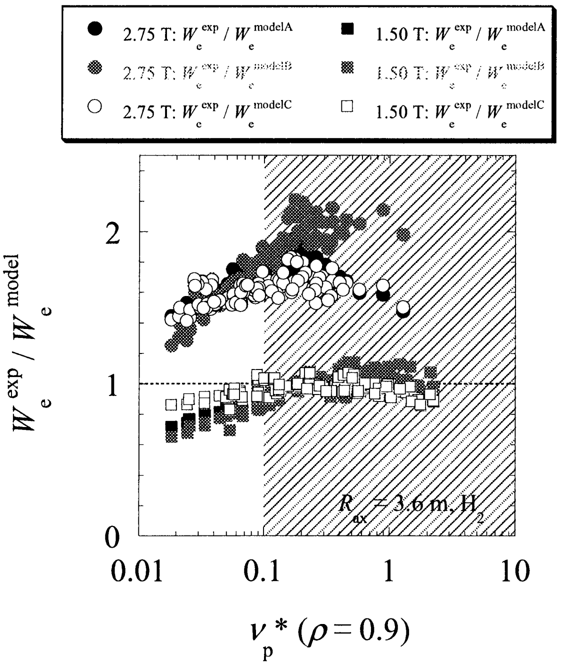

Fig. 7 Comparisons between the experimental data of W_e^{exp} and models A, B, and C. Two hydrogen datasets of different B_0 but identical R_{ax} are shown. The model C well reproduces W_e^{exp} at B_0 = 1.5 T, in the hatched region of $\nu_p*(\rho = 0.9) > 0.1$.

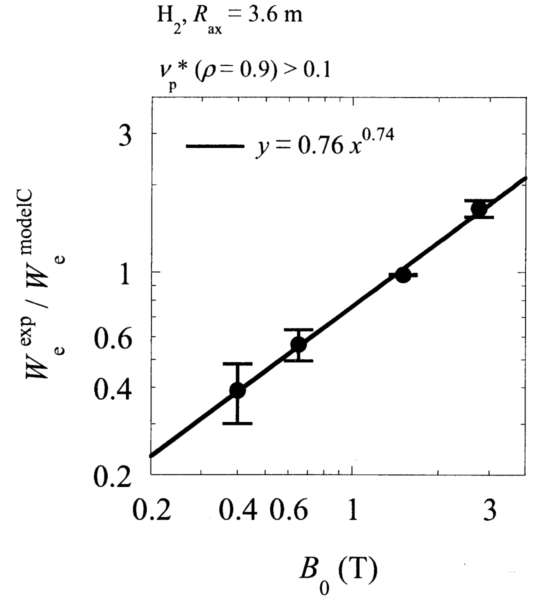

Fig. 8 Hidden dependence on the magnetic field strength of model C.

$$p_e^{\mathrm{modelD}}(\rho) = f_B f_n f_P^Q \exp(-g)\,, \tag{14}$$

$$W_e^{\mathrm{modelD}} = f_B f_n f_P^Q W_e^{\mathrm{base}}\,. \tag{15}$$

This model well reproduces W_e^{exp} in the high collisionality regime at R_{ax} = 3.6 m, regardless of B_0. At different B_0, the density region in which $\nu_p*(\rho = 0.9) > 0.1$ is not necessarily the same. For example, $\nu_p*(\rho = 0.9) = 0.1$ corresponds to $\bar{n}_e$

~ 3×10^{19} m^{-3} for B_0 = 1.5 T and $\bar{n}_e$ ~ 6×10^{19} m^{-3} for B_0 = 2.75 T, in Fig. 7. This suggests that the collisionality is more important than the density alone in determining the parameter regime where the frozen profile appears. This is why we adopted ν_p* as an abscissa in Fig. 7 instead of the density. However, the reason why the profile becomes frozen in $\nu_p*(\rho = 0.9) > 0.1$ is still an open question. The boundary between the plateau and the banana regimes lies at $\nu_p*(\rho = 0.9)$ ~ 0.06 in R_{ax} = 3.6 m and is slightly smaller than 0.1.

5. Outward-shifted Configuration

Up to this point, plasmas in the standard magnetic configuration of R_{ax} = 3.6 m have been analyzed. In this section, another dataset of the outward-shifted configuration, R_{ax} = 3.75 m, is introduced. The two configurations at the same B_0 (= 1.5 T) are compared in Fig. 9. In the low collisionality regime, W_e^{exp}/W_e^{modelD} at R_{ax} = 3.75 m decreases as the collisionality decreases. This qualitative behavior resembles that of the standard configuration, although the degradation is much enhanced. In the high collisionality regime, W_e^{exp}/W_e^{modelD} increases to ~ 0.8. In other words, the energy confinement time in R_{ax} = 3.75 m is ~ 20 % smaller than that in R_{ax} = 3.6 m even in this regime.

Electron pressure profiles at various collisionalities are compared with model D in Fig. 10, where time slices A1 – A4 are chosen from R_{ax} = 3.6 m, and B1 – B4 are chosen from R_{ax} = 3.75 m (see also Fig. 9). In the low collisionality regime at R_{ax} = 3.6 m (A1), the electron pressure is lower than model D, especially at the plasma core. The electron pressure increases as the collisionality increases (A2). In the high-collisionality regime (A3 and A4), good agreement between p_e and p_e^{modelD} is obtained, and therefore the p_e profile is frozen. Qualitatively a similar tendency is also observed in the outward-shifted configuration, where p_e is smaller than p_e^{modelD} in the low collisionality regime (B1 and B2) and increases as the collisionality increases (B3 and B4). Independent of R_{ax}, p_e at the core is smaller than the prediction of model D in the low collisionality regime and increases as the collisionality increases, while p_e at the edge is well reproduced by model D even in the low collisionality regime.

6. Discussions

It has been shown that the electron pressure profiles in LHD converge to the model profile in the high-collisionality regime. In the low-collisionality regime, the models overestimate the electron pressure profiles. There are two possible causes. One is that the profile is not yet frozen, and another is that the power and/or the density dependence in our models are not applicable in the low collisionality regime. Radial profiles of L_p, $L_n = (-\mathrm{d}(\ln n_e)/\mathrm{d}\rho)^{-1}$, and $L_T = (-\mathrm{d}(\ln T_e)/\mathrm{d}\rho)^{-1}$, are shown in Fig. 11, where time slices of A1 – A4 and B1 – B4 are chosen as Figs. 9 and 10. In the case of R_{ax} = 3.75 m, the L_p profile is not frozen at low collisionality (B1 – B2), as shown in Fig. 11(a). In the case of R_{ax} = 3.6 m, the L_p profile seems to be frozen within the scatter of the data, even in the low collisionality regime (A1 – A2), where W_e^{exp} is lower than the prediction of model D. Therefore, the heating power and/or the density dependence in the model might not be applicable in this case. The energy confinement time predicted by model D has the form of

$$\tau_E \propto \bar{n}_e^{0.28} P_{abs}^{-0.43} B_0^{0.74}, \qquad (16)$$

where it is assumed that the beam deposition profile is fixed and the radiation loss is negligibly small. It should be noted that the energy confinement time in the low-collisionality regime is well reproduced by the ISS95 scaling, which has stronger positive density dependence and stronger power degradation ($\tau_E^{ISS95} \propto \bar{n}_e^{0.51} P_{abs}^{-0.59} B_0^{0.83}$) than our model.

In this study, the confinement property of gas-fueled plasmas has been discussed. The density profiles sustained by gas puffing are basically flat except the edge region as was shown in Fig. 10. Indeed, the electron density gradient (Fig. 11(b)) is much smaller than that of the electron temperature gradient (Fig. 11(c)). Therefore, it is possible to attribute the frozen pressure profile to the property of the electron temperature gradient. To support this idea, it should be pointed out that even at low-collisionality where the L_p profile is not frozen (B1 – B2), the L_T profile seems to be frozen within the scatter of the data. However, the electron temperature profile alone is not enough to discuss the energy confinement property and it is necessary to estimate the local thermal diffusivity. After that, frozen temperature profiles can lead to a discussion of the temperature dependence of the thermal diffusivity, which is left for future study.

The frozen pressure profile appears in the low-temperature (high-collisionality) regime in LHD. At this point, our result is contrastive to the stiffness in L-mode tokamaks that appears in the high-temperature regime [16]. The electron temperature gradient mode (ETG) is one of the most probable

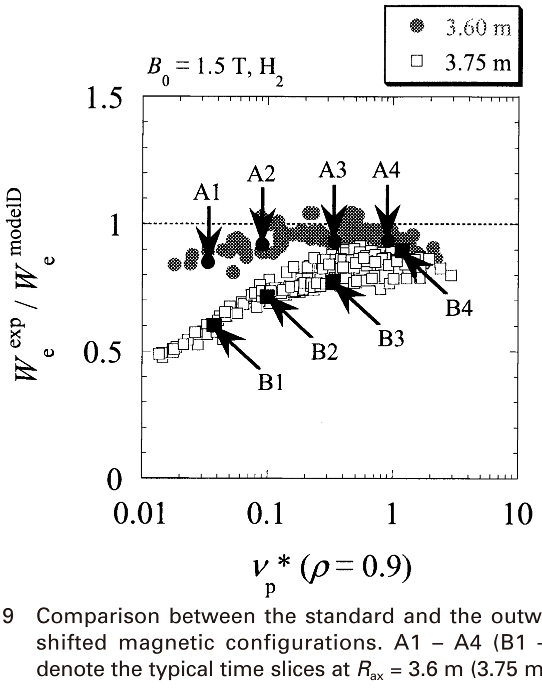

Fig. 9 Comparison between the standard and the outward-shifted magnetic configurations. A1 – A4 (B1 –B4) denote the typical time slices at R_{ax} = 3.6 m (3.75 m).

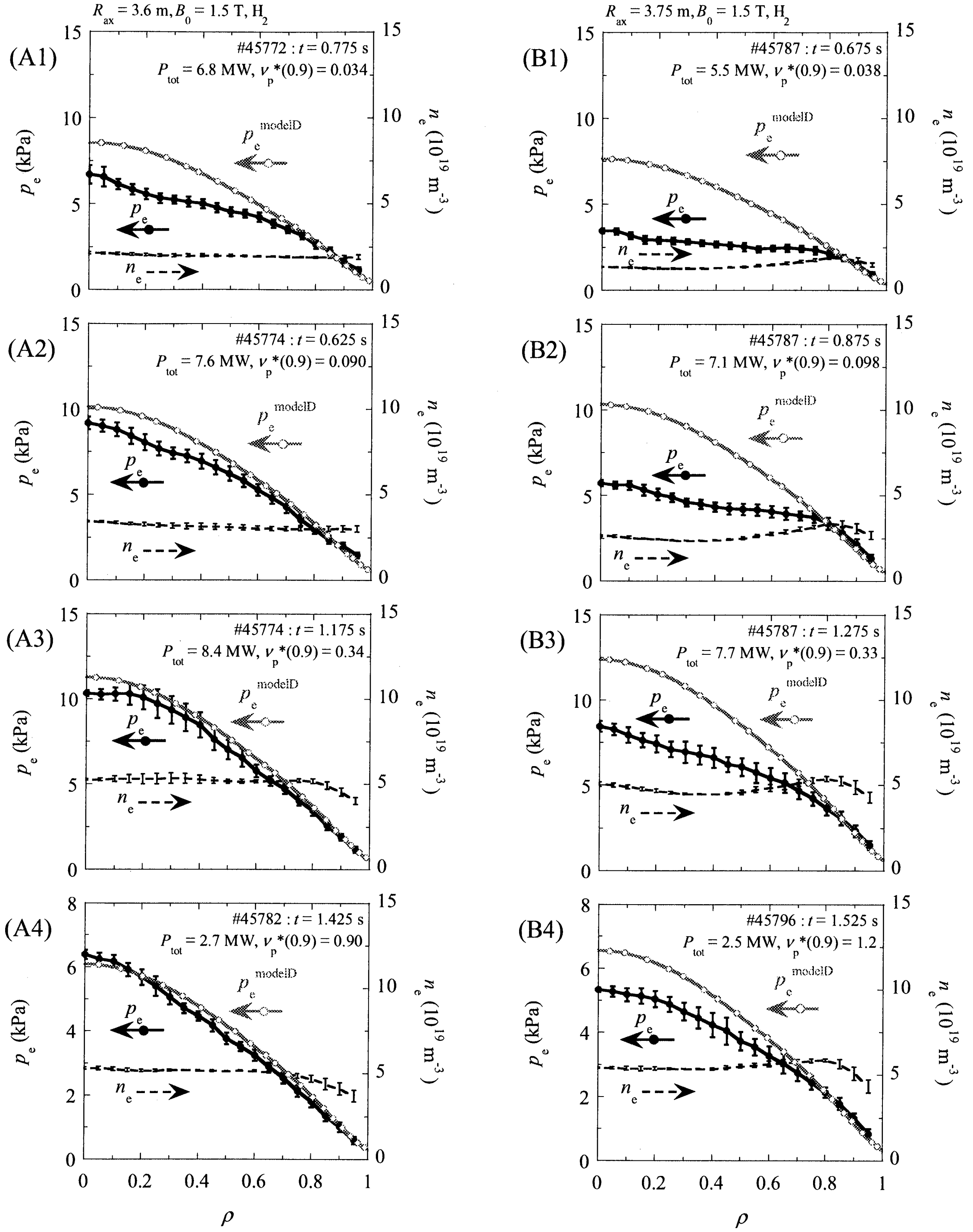

Fig. 10 Radial profiles of the electron pressure, model D, and the electron density. Indices of (A1) – (A4) and (B1) – (B4) correspond to those in Fig. 9.

candidates causing stiffness in L_T in tokamaks. In this scenario, χ increases with $T_e^{1.5}$ [36] (the collisionless trapped electron mode (TEM) also predicts a similar temperature dependence [37]), which is in good agreement with tokamak experiments [16]. The T_e dependence of χ causing the frozen profile should be much weaker than this, however, to explain the weak density dependence in Eq. (16). Although it is unknown if the thermal diffusivity can be expressed by a single parameter, let us assume here that $\chi \propto T_e^{\alpha}$. Then the expected energy confinement time scales with

$$\tau_E \propto (n/P)^{\frac{\alpha}{1+\alpha}}, \tag{17}$$

where n and P are the density and the heating power, respectively. Therefore, α ~ 0.39 is necessary to obtain the density dependence in Eq. (16). On the other hand, the power dependence in Eq. (16) is reproduced by α ~ 0.75. To reproduce both dependences simultaneously, α ~ 0.6±0.2 might be the plausible temperature dependence of χ. Anyhow, it is much weaker than the temperature dependences of α = 1.5 in existing anomalous transport models such as the gyro-

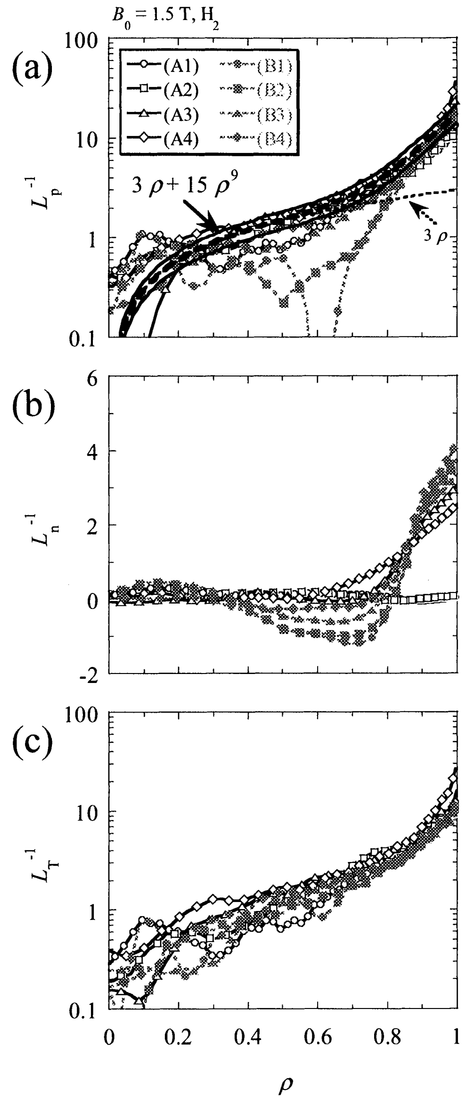

Fig. 11 Radial profiles of the characteristic length of (a) the electron pressure gradient, (b) the electron density gradient, and (c) the electron temperature gradient. Indices of (A1) – (A4) and (B1) – (B4) corresponds to those in Figs. 9 and 10.

Bohm, ETG, and TEM, and even weaker than the Bohm model (α = 1). Therefore, our result does not contradict the small stiffness factor ($\chi^{\mathrm{HP}} \sim \chi^{\mathrm{PB}}$), which rules out the strong temperature gradient dependence of χ, found in former studies in stellarators [19,21].

7. Summary

In the standard configuration of R_{ax} = 3.6 m in LHD, the electron pressure profiles of gas-fueled NB heated plasmas dominated by electron heating can be reproduced within ±10 % by the model equation of $p_{\mathrm{e}}^{\mathrm{modelID}}(\rho) = f_{\mathrm{B}}\, f_{\mathrm{n}}\, f_{\mathrm{P}}^{\mathrm{Q}} \exp(-g(\rho))$, in the high-collisionality regimes ($\nu_{\mathrm{p}}{}^*(\rho = 0.9) > 0.1$). This model consists of the frozen profile, positive dependence on the heating power, the electron density, and the magnetic field strength. Use of $f_{\mathrm{P}}^{\mathrm{Q}} = 42(Q_{\mathrm{NB}}^{\mathrm{avg}})^{0.57}$ is necessary to include the NB deposition profile effect. The global energy confinement time in the high-collisionality regimes has a weaker density dependence of $\tau_{\mathrm{E}} \propto \bar{n}_{\mathrm{e}}^{0.28}$ together with the mitigated power degradation of $\tau_{\mathrm{E}} \propto P^{-0.43}$, compared with ISS95 scaling ($\tau_{\mathrm{E}}^{\mathrm{ISS95}} \propto \bar{n}_{\mathrm{e}}^{0.51}\, P^{-0.59}$). The frozen profile discussed in this study is defined as having a gradient of the electron pressure (temperature) that is proportional to the local electron pressure (temperature) itself. This leads to an idea that the local heat diffusivity is a function of local parameter(s), such as the temperature or its gradient, which are closely connected to each other. Parameter dependences of the energy confinement time obtained here suggest a weak temperature dependence of the thermal diffusivity as $\chi \propto T_{\mathrm{e}}^{0.6\pm0.2}$. As the collisionality decreases, the electron pressure profile becomes smaller than that predicted by the model. This degradation is significant at the plasma core region and enhanced in the outward-shifted configuration of R_{ax} = 3.75 m.

References

[1] U. Stroth, Plasma Phys. Control. Fusion **40**, 9 (1998).
[2] O. Gruber *et al.*, Nucl. Fusion **41**, 1369 (2001).
[3] H. Yamada *et al.*, Nucl. Fusion **43**, 749 (2003).
[4] H. Yamada *et al.*, J. Plasma Fusion Res. SERIES **5**, 570 (2002).
[5] U. Stroth *et al.*, Nucl. Fusion **36**, 1063 (1996).
[6] A.Iiyoshi *et al.*, Nucl. Fusion **3**, 1245 (1999).
[7] O. Motojima *et al.*, Phys. Plasmas **6**, 1843 (1999).
[8] M. Fujiwara *et al.*, Plasma Phys. Control. Fusion **41**, B157 (1999).
[9] A. Komori *et al.*, Plasma Phys. Control. Fusion **42**, 1165 (2000).
[10] H. Yamada *et al.*, Phys. Rev. Lett. **84**, 1216 (2000).
[11] J. Stober *et al.*, Plasma Phys. Control. Fusion **42**, A211 (2000).
[12] M. Kotchenreuther *et al.*, Phys. Plasmas **2**, 2381 (1995).
[13] A. Dimits *et al.*, Phys. Plasmas **7**, 969 (2000).
[14] J.C. DeBoo *et al.*, *29th EPS Conference on Plasma Phys. and Contr. Fusion Montreux*, 17-21 June 2002, ECA Vol. 26B, P-2.064 (2002).
[15] F. Ryter *et al.*, Phys. Rev. Lett. **86**, 2325 (2001).
[16] F. Ryter *et al.*, Phys. Rev. Lett. **86**, 5498 (2001).
[17] N.J. Lopes Cardozo, Plasma Phys. Control. Fusion **37**, 799 (1995).
[18] H. Ringler *et al.*, Plasma Phys. Control. Fusion **32**, 933 (1990).
[19] L. Giannone *et al.*, Nucl. Fusion **32**, 1985 (2002).
[20] U. Stroth *et al.*, *Proc. Workshop on Local Transport Studies in Fusion Plasmas* (Varenna 1993), 161 (1994).
[21] H.J. Hartfuss *et al.*, Plasma Phys. Control. Fusion **36**, B17 (1994).
[22] T. Shimozuma *et al.*, Plasma Phys. Control. Fusion **45**, 1183 (2003).
[23] K. Ida *et al.*, Phys. Plasmas **11**, 2551 (2004).
[24] S. Inagaki *et al.*, Plasma Phys. Control. Fusion **46**, A71 (2004).
[25] S. Murakami *et al.*, Nucl. Fusion **42**, L19 (2002).
[26] S. Murakami *et al.*, J. Plasma Fusion Res. SERIES **5**,

620 (2002).

[27] M. Okamoto *et al.*, Plasma Phys. Control. Fusion **41**, A267 (1999).

[28] Annual Report of National Institute for Fusion Science, April 2003 - March 2004.

[29] M. Osakabe *et al.*, Rev. Sci. Instrum. **72**, 590 (2001).

[30] S. Murakami, N. Nakajima, M. Okamoto, Trans. Fusion Technology **27**, 256 (1995).

[31] K. Narihara *et al.*, Phys. Rev. Lett. **87**, 135002 (2001).

[32] K. Kawahata *et al.*, Rev. Sci. Instrum. **70**, 707 (1999).

[33] S.P. Hirshman, W. Van Rij and P. Merkel, Comput. Phys. Commun. **43**, 143 (1986).

[34] S. Sudo *et al.*, Nucl. Fusion **30**, 1 (1990).

[35] Y. Xu *et al.*, Nucl. Fusion **42**, 601 (2002).

[36] F. Jenko *et al.*, Phys. Plasmas **7**, 1904 (2000).

[37] D.F. Düchs *et al.*, in Plasma Physics and Controlled Nuclear Fusion Research 1986, *Proceedings of the 10th International Conference*, Kyoto (IAEA, Vienna) vol. 1, 325 (1987).